Automotive Experiences
Vol. 7 No. 3 (2024) pp. 552-566
p-ISSN: 2615-6202 e-ISSN: 2615-6636

Research Paper

Thermal Performance Enhancement of Serpentine Cooling Design Using Branch Modification for Lithium-Ion Batteries

Arya Rafi Abrari[1, 7], Teguh Hady Ariwibowo[2, 7], Dadet Pramadihanto[3, 7], Nu Rhahida Arini[2], Eko Henfri Binugroho[4, 7], Akio Miyara[5, 6]

1Department of Electrical Engineering, Politeknik Elektronika Negeri Surabaya, 60111, Indonesia
[2]Department of Power Plant Engineering, Politeknik Elektronika Negeri Surabaya, 60111, Indonesia
[3]Department of Computer Engineering, Politeknik Elektronika Negeri Surabaya, 60111, Indonesia
[4]Department of Mechatronics Engineering, Politeknik Elektronika Negeri Surabaya, 60111, Indonesia
[5]Department of Mechanical Engineering, Saga University, 840-8502, Japan
[6]International Institute for Carbon-Neutral Energy Research, Kyushu University, 819-0395, Japan
[7]Center for Research and Innovation on Advanced Transportation Electrification, Politeknik Elektronika Negeri Surabaya, 60111, Indonesia

teguhhady@pens.ac.id

https://doi.org/10.31603/ae.12709

Published by Automotive Laboratory of Universitas Muhammadiyah Magelang

Article Info
Submitted: 24/11/2024
Revised: 16/12/2024
Accepted: 17/12/2024
Online first: 19/12/2024

Abstract

Lithium iron phosphate (LiFePO4) batteries offer preferences as well as low cost, safety, environmental compatibility, and firmness over repeated cycles. However, when subjected to high currents, this battery generates thermal issues, particularly when arranged in packs. This study aims to maintain the LiFePO4 80Ah battery within an optimal temperature range (20 °C – 40 °C) while minimising pumping power. The proposed research introduces a serpentine channel with additional branches. The design variations include a gradient in branch spacing and changes in channel width. Each design is evaluated using dimensionless parameters representing maximum temperature, temperature uniformity, pumping power, and cooling efficiency coefficient. The best design from each variation is then compared with the conventional serpentine (CS) channel design, which is well-known for its superior thermal performance. The gradient variation reduces $T_{max}{}^*$ and T_σ by 0.07 and by 0.42, respectively, compared to the non-gradient channel design, at a Re 400 and a 3 C C-rate. The design with the largest channel width reduces $T_{max}{}^*$ by 0.57 or 11.32 °C compared to the design with the smallest channel width. At a Re 1000 and 3 C C-rate, the reduction in $T_{max}{}^*$ for the proposed channel design compared to the CS design is 0.017. In terms of the friction factor (f), the proposed design is 0.0149 lower than the CS design. The findings show that the proposed channel design outperforms the CS design in thermal performance while requiring less pumping power.

Keywords: Lithium-ion battery; Battery thermal management system; Liquid cooling plate; Serpentine channel; Mini-channel; Cooling performance

1. Introduction

The development and utilisation of environmentally friendly energy continue to grow across various industrial sectors, aiming to reduce the negative environmental impact caused by carbon emissions [1]–[4]. Transitioning from internal combustion engine (ICE) vehicles to electric vehicles is one strategy to address this challenge [5]. In electric vehicles, the battery is a critical component. It serves as the energy source, similar to the engine in ICE vehicles [5]–[7]. Lithium iron phosphate (LiFePO4) batteries offer preferences as well as cheap, security, environmental compatibility, and firmness over repeated cycles [8]. When in operation, the battery produces heat as it undergoes charging and discharging cycles. The use of a battery operating at high currents can lead to serious thermal issues, especially when arranged in a pack [9], [10]. The ideal operating temperature for the battery is between 20 °C and 40 °C, with a maximum temperature difference between cells of minus than 5 °C [11]–[13]. Therefore, this type of battery has received considerable attention for improving performance and reliability under extreme conditions, particularly in relation to its thermal behavior [12], [14], [15].

Numerous battery cooling methods, including air cooling, liquid cooling, and phase change materials (PCM), have been developed for EVs and HEVs in recent years [16], [17]. So far, liquid cooling is the most efficient technique due to its high thermal conductivity compared to other cooling methods [18]. The most widely applied liquid cooling methods for batteries include direct-contact and indirect-contact approaches. Direct-contact is a method where the cooling fluid (dielectric heat transfer fluid) directly contacts the battery, making it more efficient. However, it comes with higher practical challenges [18]. On the other hand, indirect-contact liquid cooling uses channels within a metal material, commonly referred as cold plate [19]. In terms of thermal performance, indirect-contact liquid cooling is slightly less efficient than direct-contact cooling. Still, it is more practical for electric vehicles, making it an interesting subject for research [11], [18]–[20]. Improvements to the cold plate generally focus on enhancing heat transfer and reducing the pumping power required [21]. Minichannel cold plates have significant potential due to their excellent temperature distribution, lightweight, compact design, and high heat dissipation capability [22]–[24]. Serpentine channels are known for their excellent thermal performance and temperature distribution [25], [26]. Previous research discusses various serpentine channel designs and compares their performance. The findings reveal that serpentine channels deliver the most effective thermal performance, albeit at the cost of higher pumping power [20]. Deng et al. [27] delved into various serpentine channel structures in cold plates. The study's results indicate that modifying the serpentine channel structure reduced the maximum temperature by up to 26 °C compared to other serpentine channel configurations analysed. Liu et al. [25] enhanced the performance of serpentine channels by introducing intersections into the channel design. The study results show that adding intersections helps reduce pumping power beside conventional serpentine channels. Jaffal et al. [28] studied serpentine channels with added ribs. The results indicate that the replenishment of ribs could increase the Nusselt number by up to 71% and the friction factor by up to 151% compared to channels without ribs. Sun et al. [29] studied branched serpentine channel structures. The results showed that using the branched structure could reduce the average temperature and pressure drop. Wang et al. [30] performed a multi-objective optimisation study on serpentine channels to achieve maximum performance. Using a multi-objective genetic algorithm (MOGA), the new channel design reduced the maximum pressure by up to 13.28%. Fan et al. [31] suggested incorporating secondary flow to enhance the thermal performance of serpentine channels. Although the cooling performance of the proposed channel design was lower than that of the conventional serpentine, it successfully reduced pumping power by up to 92.6%. However, despite the various studies, the thermal performance achieved is still considered unsatisfactory. To the best of the author's knowledge, no modifications to serpentine channel designs for EV battery cooling have achieved thermal performance equal to or better than that of the conventional serpentine (CS) design. The proposed research introduces a serpentine channel with additional branches to reduce pump power [25], [29], [31].

This study aims to ensure the EV battery operates within ideal conditions while minimising pumping power. This study is inspired by previous research that demonstrated an improvement in performance with the introduction of flow dividers, although some limitations remain [25], [31]. This study explores various channel designs to understand the characteristics of each design. The channel design variations include changes in branch spacing to form a gradient and variations in channel width. Gradient variations are utilised to improve the thermal performance of the channel at the same pump power [25], [32]. Conversely, channel width variations demonstrate a sensitivity on reducing the serpentine channel's maximum and average temperature [30]. After determining the best channel design from each variation, the proposed design is compared with the conventional serpentine (CS) design. Each channel design is evaluated based on dimensionless parameters representing maximum temperature, temperature uniformity, pumping power, and cooling efficiency coefficient. This study is expected to produce results that align with the hypothesis and address the research gap by offering solutions for battery thermal management systems in electric vehicles.

2. Methods

2.1. CFD Modelling

The battery utilised in this study is a prismatic lithium iron phosphate ($LiFePO4$) battery with an 80Ah capacity [33]. The dimensions of each battery cell are 166 mm x 130 mm x 37 mm. The characteristics of the battery are shown in **Table 1**. The developed battery module is arranged as shown in **Figure 1**. The cooling plate with integrated serpentine channels is located between the battery cells. The dimensions of the cooling plate have a thickness of 6 mm, with the length and width of the plate matching the shape of the two batteries. The serpentine channels used have a rectangular cross-section, with a height of 2 mm and a varying width from 6 mm to 10 mm.

To minimise computational costs, the case is simplified by modelling a cooling plate with serpentine channels. The simulation is conducted under steady-state conditions to analyse the plate's behaviour in a saturated thermal state [20]. The simulation domain consists of two regions: aluminium plate and water as the working fluid. The cooling plate made of aluminium is assumed to have homogeneous and isotropic material properties, while the coolant fluid is assumed to be incompressible with constant properties. The material properties are written in **Table 2** [34]. **Figure 1a** shows the simulated cooling plate placed at the centre of the battery module. **Figure 1b** illustrates how heat generated by the batteries flows to the plate through conduction. The heat is then transferred to the coolant fluid through convection. At the tight space between the battery cells, the cooling plate absorbs the heat and shares it with the cooling plate on the opposite side. In this case, one side of the cooling plate absorbs half of the heat generated by the batteries. Symmetry boundary condition is applied to shorten the simulation time while maintaining similar conditions. The geometry used in this simulation is shown in **Figure 2**. The serpentine channel is divided into several branches as shown in **Figure 2a**. Detailed dimensions of the geometric variations are provided in **Table 3**. The first geometric variation is the spacing between the serpentine branches. The spacing between the branches forms a gradient. The next geometric variation is increasing the height-to-width ratio of the rectangular pipe. The height of the pipe is constant, so to increase the ratio, the pipe width (D) is varied. **Figure 2b** shows the geometry of the conventional serpentine (CS) channel for comparison.

2.2. Mathematical Equation and Data Reduction

The fluid flow within the plate is determined by the continuity equation and the momentum Equation (1) and Equation (2) [35].

$$\nabla\vec{v} = 0 \tag{1}$$

$$-\frac{1}{\rho_w}\nabla P + \mu_w(\nabla^2\vec{v}) = \frac{\partial\vec{v}}{\partial t} + \vec{v}(\nabla\vec{v}) \tag{2}$$

where $\vec{v}$ is the velocity vector of the fluid flow; ρ_w is the fluid density (water); P is the static pressure; and μ_w is the fluid viscosity. The coolant energy equation is shown in Equation (3) [35].

Table 1. Battery specification

Parameter	Value
Capacity (Ah)	80
Nominal voltage (V)	3.2
Maximum voltage (V)	3.6
Maximum charge current (C)	1
Maximum discharge current (C)	3
Maximum continuous discharge current (C)	1
AC impedance resistance (mΩ)	≤0.5
Weight (g)	1630

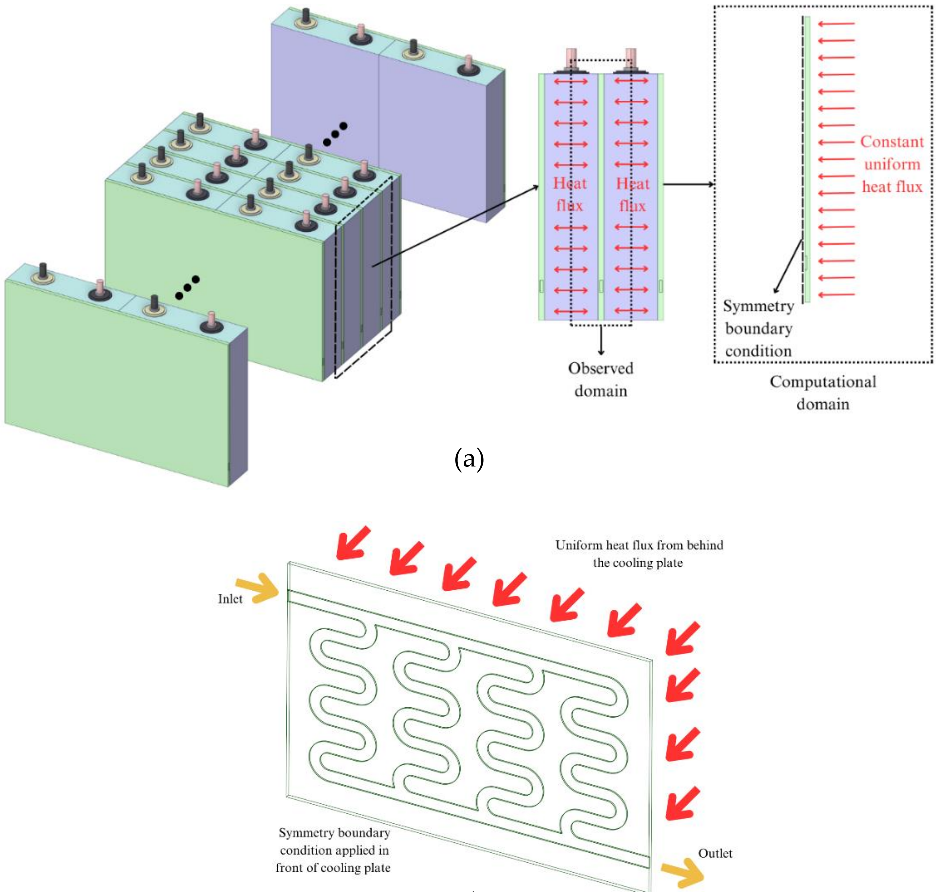

(b)

Figure 1. Simulation conditions: a) simulation approach diagram, and b) simulation details

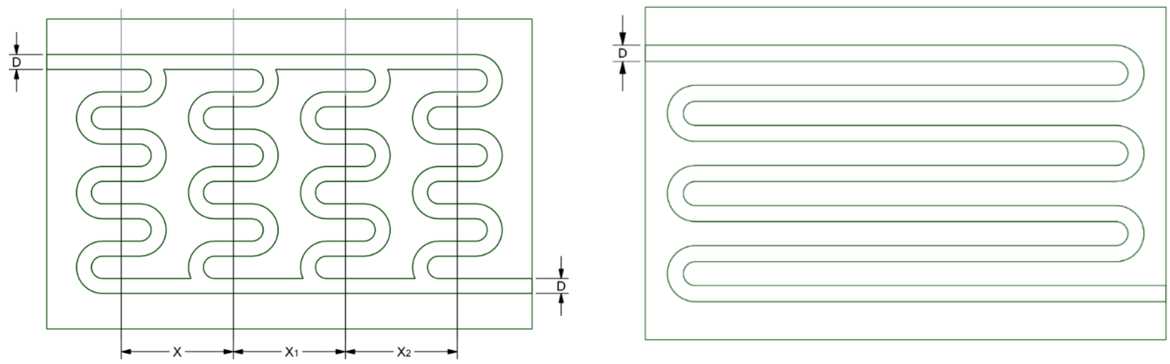

(a) (b)

Figure 2. Simulation geometry: a) serpentine channel with branches, and b) conventional serpentine (CS)

Table 2. Thermophysical properties of materials

Parameter	Value
Coolant fluid	Liquid water
Density (Kg/m^3)	998.16
Specific heat (J/KgK)	4184.36
Thermal conductivity (W/mK)	0.6
Viscosity (Kg/ms)	0.00100163
Plate material	Aluminum
Density (Kg/m^3)	2702.0
Specific heat (J/KgK)	903.0
Thermal conductivity (W/mK)	237.0

Table 3. Geometry specifications

Channel design	X (mm)	X1 (mm)	X2 (mm)	D (mm)
Initial	60	60	60	8
CS	-	62	-	8
Gradient-1	64	62	54	8
Gradient-2	66	62	52	8
Gradient-3	68	62	50	8
Width-1	60	60	60	6
Width-3	60	60	60	10

$$\rho_w c_{p,w} \frac{\partial T_w}{\partial t} + \nabla\left(\rho_w c_{p,w} \vec{v} T_w\right) = \nabla(k_w \nabla T_w) \quad (3)$$

where $c_{p,w}$, k_w, and T_w, are the specific heat capacity of water, thermal conductivity of water, and water temperature, respectively. The energy equation for the aluminium plate is given as shown in Equation (4) [35].

$$\rho_s C_{p,s} \frac{\partial T_s}{\partial t} = k_s \nabla^2 T_s \quad (4)$$

where $C_{p,s}$, k_s, and T_s, are the specific heat capacity of aluminium, the thermal conductivity of aluminium, and the temperature of the aluminium, respectively. When the vehicle operates, the heat generated by the battery is determined using the following Equation (5) [36].

$$Q_b = I(U_{ocv} - U) - IT_b \frac{dU_{ocv}}{dT_b} \quad (5)$$

where Q_b is the heat generated by the battery; U_{ocv} is the open-circuit voltage; U is the battery voltage; and $IT_b \frac{dU_{ocv}}{dT_b}$ is the entropy coefficient resulting from electrochemical reactions within the cell. The open-circuit voltage is assumed to be equal to the maximum battery voltage, and the entropy coefficient is neglected due to its small value [37], [38]. In this research, the heat generated by the battery is approximated using a uniform heat flux utilised to the back surface of the cooling plate. The heat flux equation is shown in Equation (6).

$$q'' = \frac{Q_b}{A} \quad (6)$$

where A is the contact area between the plate and the battery cell. The heat flux generated by the battery is 832.19 W/m², 1664.37 W/m², and 2496.56 W/m² for C-rates of 1 C, 2 C, and 3 C, respectively.

The flow rate in this study is calculated based on the Reynolds number (Re). Generally, minichannel flows exhibit a low Reynolds number [27], [31]. This study uses variations of Re values ranging from 400 to 1200. Since Re values are below 2300, the simulation applies a laminar flow model. Re and D_h are calculated using the following Equations (7) and (8).

$$Re_D = \frac{\rho_w v D_h}{\mu_w} \quad (7)$$

$$D_h = \frac{4A_c}{P} \quad (8)$$

where D_h is the hydraulic diameter; A_c is the cross-sectional flow area; and P is the wetted perimeter.

During the simulation, several data points were collected to represent the maximum temperature, temperature uniformity, and the required pumping power of the cooling plate. The maximum temperature on the surface of the plate can indicate conditions that approach the operating state of the batteries [27], [39]. Equation (9) represents the maximum temperature in a dimensionless parameter.

$$T_{max}{}^* = \frac{T_{max}}{T_{ref}} \quad (9)$$

where T_{max} is the maximum temperature on the surface of the plate; and T_{ref} is the reference temperature, which in this case is the inlet temperature of 20 °C. Temperature uniformity is approximated using the standard deviation of the temperature. A smaller standard deviation value indicates a more uniform temperature distribution of the batteries inside the pack [27], [39]. The standard deviation is calculated using the Equations (10) and (11) [27].

$$T_\sigma = \sqrt{\frac{\int \left(T - T_{avg}\right)^2 dA}{\int dA}} \quad (10)$$

$$T_{avg} = \frac{\int T dA}{\int dA} \quad (11)$$

where T_{avg} is the average temperature of the surface subjected to heat flux. Pumping power is approximated using the friction factor. The friction factor is determined using the Equation (12) [40].

$$f = \Delta P \frac{2D_h}{v^2 \rho L} \tag{12}$$

where ΔP is the pressure difference between the inlet and outlet; and L is the length of the channel. The dimensionless parameter to represent the cooling efficiency coefficient is calculated using Equation (15), which is derived from the ratio of the heat dissipated to the pumping power as shown in Equations (13) and (14), respectively [31].

$$Q_w = \dot{m}_w c_{p,w} (T_{in} - T_{out}) \tag{13}$$

$$P_w = v_{in} A_c \Delta P \tag{14}$$

$$j_w = \frac{Q_w}{P_w} \tag{15}$$

where $\dot{m}_w$ is the mass flow rate; ΔP is the pressure drop; T_{in} is the inlet temperature; and T_{out} is the outlet temperature.

2.3. *Grid Independent Test and Validation*

Meshing is the process of discretising a continuous domain into smaller computational cells, enabling the solution to be obtained through algebraic equations. In this study, a combination of structured and tetrahedral meshes is employed as illustrated in Figure 3. A structured mesh is applied in the liquid domain for high accuracy and adaptability to various cases, while a tetrahedral mesh is used in the solid/plate domain [26], [41]. A grid independence test is conducted to verify the accuracy of the simulation. The effect of the grid on $T_{max}{}^*$ is observed using the initial channel design with a discharge rate of 1 C at Re 400. Five grid variations are performed to examine the grid characteristics. Figure 4 shows that for grids with 400,000 elements and 1.2 million elements, the response of $T_{max}{}^*$ only changes slightly. However, for the next grid with 2.1 million elements, $T_{max}{}^*$ decreases drastically by 0.153.

Figure 3. Mesh model

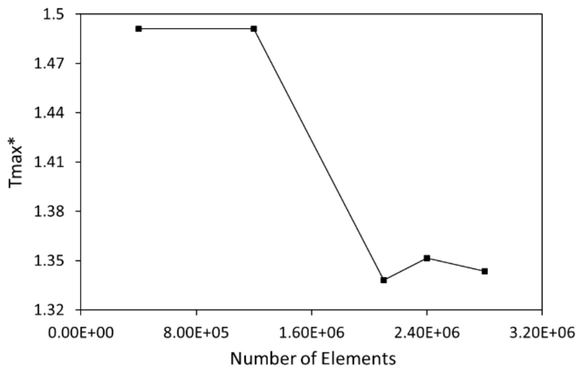

Figure 4. Grid independent test

This indicates that the grid with 1.2 million elements is not yet stable. On the other hand, grids with 2.4 million and 2.8 million elements show fluctuations but are not significant. Based on the obtained characteristics, the grid with 2.1 million elements with an average skewness of 0.25 is used for subsequent simulations.

Validation is carried out by comparing the simulation results of a single cell with experimental data obtained from a controlled test. The experiment is conducted by placing the battery in a test chamber, which is maintained at a temperature of 25 °C. Four Type-K thermocouples are placed at four points on one side of the battery. The experiment is performed at a C-rate of 0.5 C using a DC electronic load (GW-Instek PEL-3041). The average experimental temperature data are evaluated against the simulation results, yielding a root mean square error (RMSE) of 0.17.

3. Results and Discussion

3.1. *Effect of Channel Spacing Gradient*

This section discusses the effect of the gradient. Three gradient channel designs are analysed and compared with the initial channel design, which has no gradient. The influence of the gradient is observed based on C-rate and Re with respect to the observed parameters, namely $T_{max}{}^*$, T_σ, and f.

Figure 5 illustrates the characteristics of each gradient channel design variation based on C-rate and Re concerning the observed parameters, namely $T_{max}{}^*$, T_σ, and f. Figure 5a shows the differences based on $T_{max}{}^*$ for each gradient. At Re 400, the design without a gradient has the highest $T_{max}{}^*$ value of 2.16 at a C-rate of 3 C, while the lowest $T_{max}{}^*$ value is observed for gradient-1, with a value of 2.09. The difference between the non-gradient design and gradient-1 is 0.07 at Re

400 and 3 C C-rate, this corresponds to a temperature difference of 1.46 °C. When comparing the gradient designs, gradient-3 shows the highest T_{max}^* value, followed by gradient-2 and gradient-1. This phenomenon suggests that the addition of a gradient improves channel thermal performance, although it does not imply that higher gradient values always result in a higher T_{max}^* value. **Figure 6** shows the temperature contour comparison between the gradient-1 and gradient-3 designs. In **Figure 6b**, the gradient-3 channel tends to focus on the right side (near the outlet), which causes the middle region to be distanced from the channel, resulting in a hot spot. Conversely, in **Figure 6a**, gradient-1 demonstrates a lower temperature at the centre of the channel. Overall, the correlation between T_{max}^* and Re indicates that as Re increases, T_{max}^* decreases. At Re values above 800, the T_{max}^* values show similar trends across all C-rates. This phenomenon suggests that the characteristics of channels with added gradients tend to converge at higher Re. A similar finding was reported in previous studies, where the addition of a gradient improved thermal performance. However, the differences between gradient designs are more pronounced at lower flow rates or pumping powers. At higher flow rates or pumping powers, the maximum temperature values tend to become more similar across all designs [25].

Figure 5b shows the channel gradient characteristics in terms of the standard deviation of temperature. The channel design with the most uniform temperature distribution is gradient-1, followed by gradient-2, gradient-3, and the initial channel design. The difference in T_σ between the initial channel design and the gradient-1 channel design is 0.42 at Re 400 and 3 C C-rate. The T_σ response has a similar trend to the gradient channel's response in terms of T_{max}^*. At a C-rate of 1 C, the T_σ values are relatively consistent across all channel designs at the same Re. **Figure 5c** illustrates the characteristics of the friction factor (f). For all channel designs, the friction factor values remain relatively constant at the same Re, and as Re increases, the friction factor decreases. This phenomenon indicates that adding a gradient to the channel can reduce the maximum temperature and enhance temperature distribution while maintaining the same pumping power.

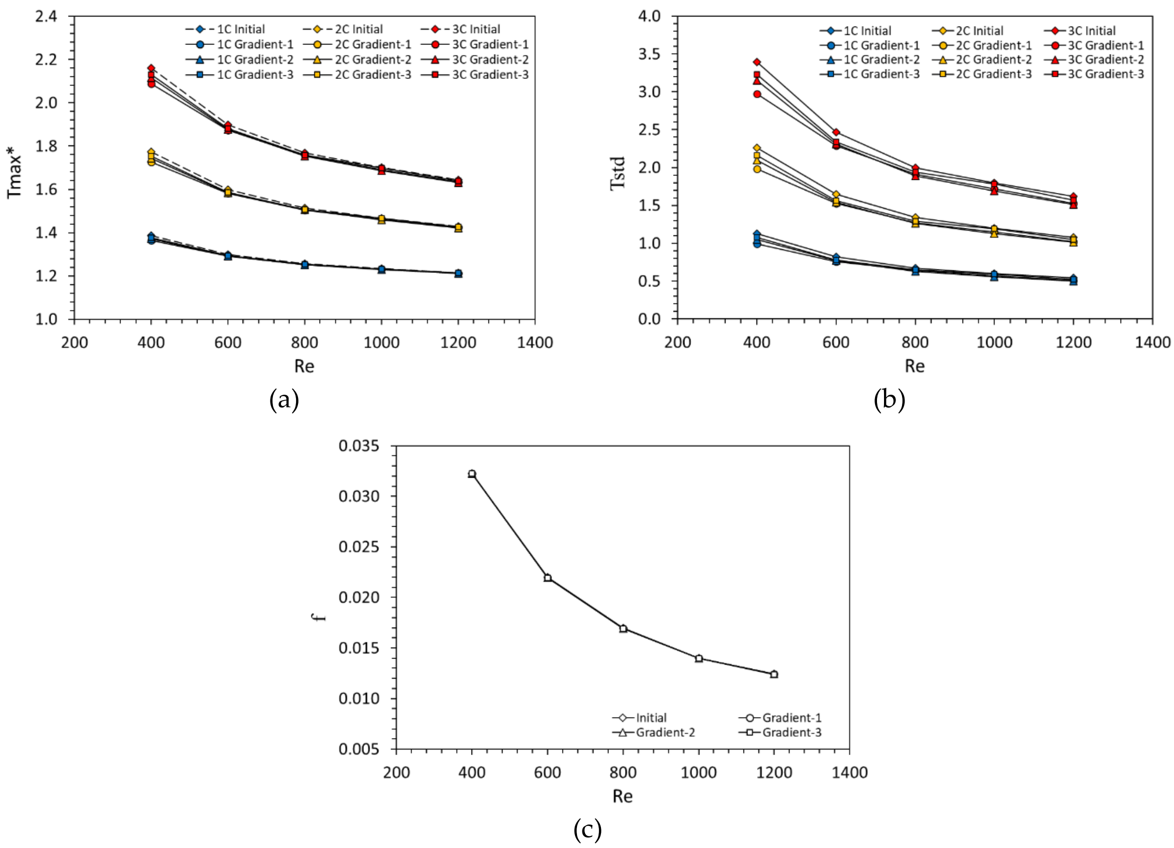

Figure 5. Effect of channel gradient on: (a) T_{max}^*, (b) T_σ, and (c) f

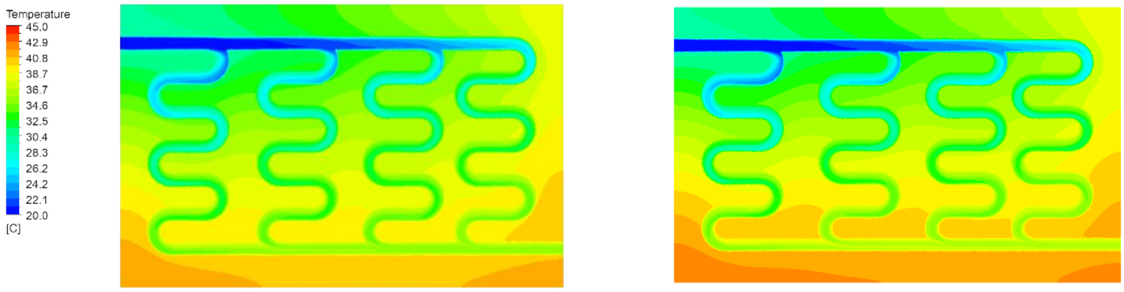

(a) (b)

Figure 6. Comparison of temperature contours at Re 400 and 3 C C-rate: (a) gradient-1 channel design, and (b) gradient-3 channel design

3.2. *Effect of Channel Width*

This section discusses the effect of channel width (D) on thermal performance and flow characteristics. **Figure 7** shows the influence of channel width on $T_{max}{}^{*}$, T_{σ}, and f. **Figure 7a** and **Figure 7b** illustrate the relationship between channel width, $T_{max}{}^{*}$ and T_{σ}. The highest to lowest $T_{max}{}^{*}$ values are observed in the width-1 design, initial design, and width-3 design. At Re 400 and 3 C C-rate, the $T_{max}{}^{*}$ difference between the width-1 and width-3 designs is 0.57, equivalent to 11.32 °C in actual temperature. The standard deviation of temperature T_{σ} at Re 400 and 3 C C-rate differs by 1.53 between the width-1 and width-3 channel designs. The width-3 design exhibits more uniform temperature distribution. This phenomenon occurs due to the influence of the height-to-width ratio of the channel. The width-3 design has the highest ratio among the other designs, which is 5. The width-1 design has the highest values for $T_{max}{}^{*}$ and T_{σ} because of its smaller ratio of 3. As the ratio increases, thermal performance improves [40]. Similarly, as Re increases, both $T_{max}{}^{*}$ and T_{σ} decrease, consistent with earlier observations [40].

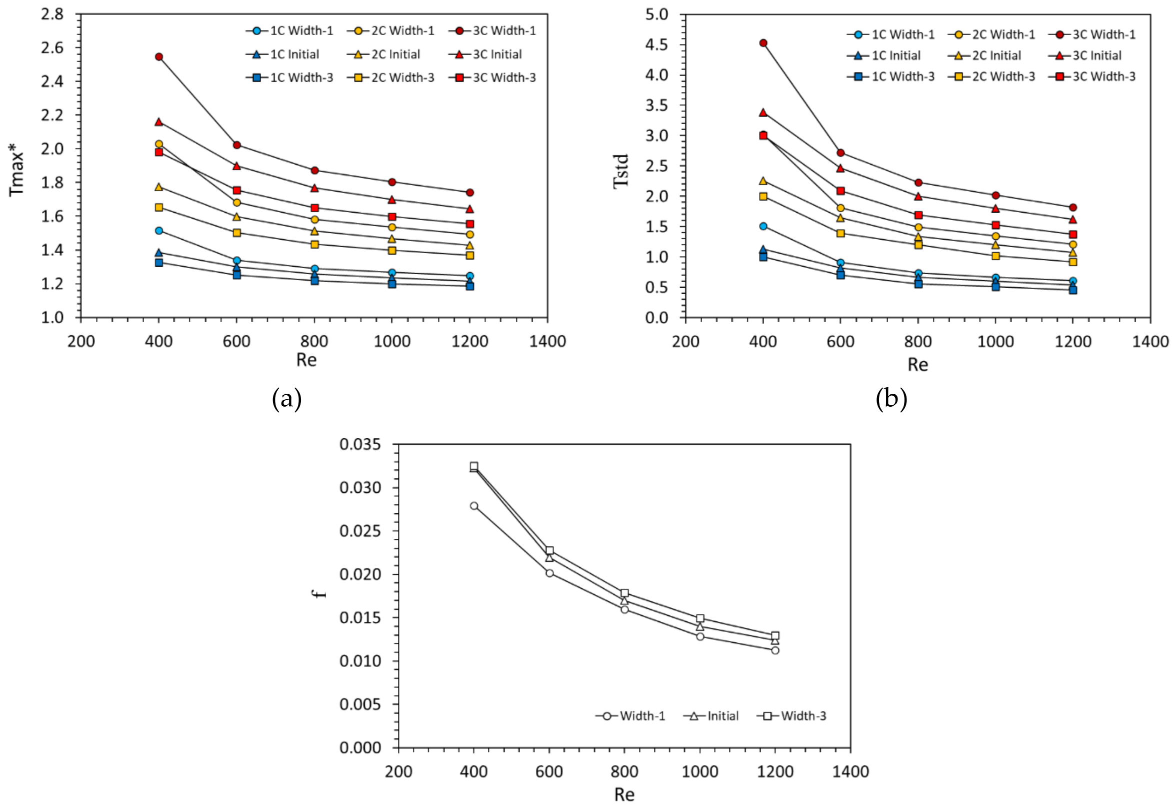

(a) (b) (c)

Figure 7. Effect of channel width on: (a) $T_{max}{}^{*}$, (b) T_{σ}, and (c) f

As shown in Figure 7c, the friction factor (f) is highest for the width-3 design, followed by the initial and width-1 designs. At Re 400, the friction factor (f) for the initial and width-3 channels shows a small difference of 0.0002, with the width-3 design having the larger value. The relationship between Re and f is inversely proportional, where increasing Re leads to a decrease in f. The smallest value of f is obtained from the width-1 design (with the smallest channel diameter ratio), which is 0.02796 at Re 400. At the same Re value, the hydraulic diameter of the width-3 channel is larger than the other designs, resulting in the smallest flow velocity. At Re 1200, the pressure drop values for the width-1, initial, and width-3 channels are 472.69 Pa, 428.04 Pa, and 393.45 Pa, respectively, indicating that wider channels reduce pressure drop. Several studies have also reported similar phenomena where increasing the channel width (D) results in a reduction of pressure drop at the same Re [30]. However, in this case, the influence of f on the channel length and hydraulic diameter are more dominant. Therefore, despite having higher $T_{max}{}^{*}$ and T_{σ} values the width-1 design offers the lowest pumping power primarily due to its smaller friction factor.

3.3. Comparison of Channel Variations

This section compares the proposed channel designs (gradient-1 and width-3) with the CS channel design based on thermal performance and flow characteristic. Gradient-1 and width-3 were selected as representatives due to their superior thermal performance. The comparison includes parameters such as $T_{max}{}^{*}$, T_{σ}, f, j_w, temperature contours, and pressure contours.

Figure 8 summarises the thermal performance and flow characteristics of the three channel designs. Figure 8a shows the variation in $T_{max}{}^{*}$ for each design. At Re 400 and 3 C C-rate, the gradient-1 design has the highest $T_{max}{}^{*}$ value, followed by width-3 and CS. At Re 400 and 3 C C-rate, the difference between the highest and lowest $T_{max}{}^{*}$ values is 0.1905, (3.78 °C). For Re above 600, the CS and width-3 channel designs show nearly the same $T_{max}{}^{*}$ across all C-rate variations. At Re 1000 and 3 C C-rate, the width-3 channel design has the smallest $T_{max}{}^{*}$ value by 1.651, which is 0.017 lower than the CS channel design. Under these conditions, the width-3 design is more reliable in maintaining the battery within its optimal operating temperature compared to the CS design. This indicates that the width-3 design is more effective at maintaining the maximum battery temperature compared to the CS design at Re >1000 with the difference not exceeding 0.001.

Figure 8b shows the characteristics of each channel design with respect to T_{σ}. At Re 400, there is a noticeable difference in T_{σ}, but the T_{σ} values for the gradient-1 and width-3 channel designs tend to be the same across all C-rate variations. Meanwhile, the CS channel design at Re 400 stands out with the smallest T_{σ} values across all C-rates. The difference in T_{σ} between the width-3 design and the CS design at Re 400 and 3 C C-rate is 1.16. Figure 10 and Figure 6a shows the temperature contours for all three channel designs at Re 400 and 3 C C-rate. In Figure 10a, the flow in the CS channel moves straight toward the plate's edge, resulting in a more uniform temperature distribution due to the absence of branches. In contrast, the gradient-1 and width-3 channel designs, as shown in Figure 6a and Figure 10b, show the flow steering towards the nearest branch from the inlet area. This flow pattern results in non-uniform temperature distributions for the gradient-1 and width-3 designs. Therefore, at low flow rates (Re 400), the CS design performs better in heat distribution. When comparing the gradient-1 and width-3 designs, the width-3 design demonstrates flow that tends to direct toward the edge, resulting in a better temperature distribution than the gradient-1 design at Re 400. At higher flow rates (Re >1000), the width-3 design matches the performance of the CS design in terms of temperature distribution. The difference in T_{σ} between the width-3 and CS designs is not bigger than 0.03, indicating a similar temperature distribution. Figure 11 shows the temperature contours at Re 1200 and 3 C C-rate. In Figure 11a, the CS channel design shows a fairly uniform temperature distribution with T_{σ} = 1.36. Figure 11b depicts the flow characteristics of the gradient-1 design, which is strong enough to reach the plate's edge. However, the gradient-1 design still shows some uneven distribution with T_{σ} = 1.53, especially in the lower part of the inlet area. This occurs because the end of the plate is far from the channel. Figure 11c displays the temperature contours for the width-3 design with T_{σ} = 1.38, demonstrating a temperature distribution similar to that of the CS design.

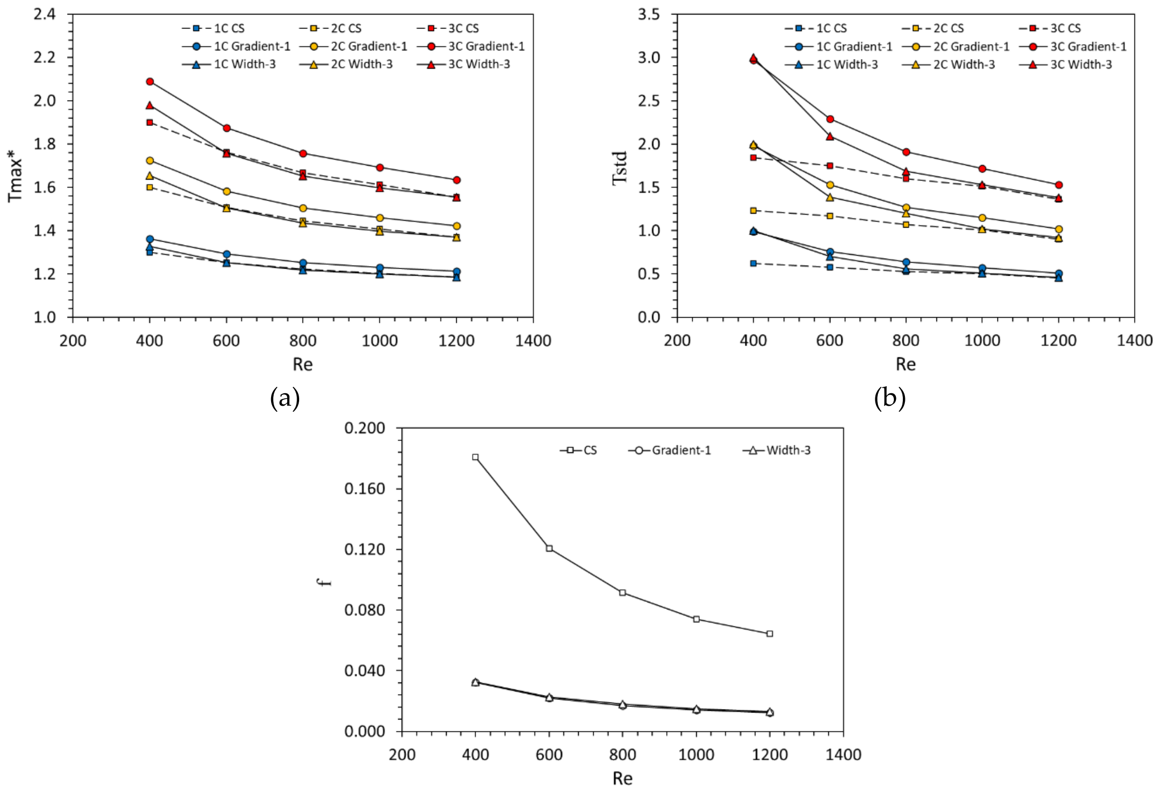

Figure 8. Comparison of channel variations: (a) effect of channel variation on $T_{max}{}^{*}$, (b) effect of channel variation on T_{σ}, and (c) effect of channel variation on f

Figure 8c shows the characteristics of each channel design with respect to the f. The values of f are arranged in descending order as follows: CS channel, gradient-1, and width-3. At Re 400, the difference in f values is quite evident, with the CS channel design having an f value of 0.181, while the values for the gradient-1 and width-3 designs are similar, around 0.033. The difference in f values is influenced by the pressure drop. The CS channel design has the highest pressure drop compared to the gradient-1 and width-3 designs. The pressure drop values for the CS, gradient-1, and width-3 designs at Re 400 are 757.96 Pa, 109.56 Pa, and 123.46 Pa, respectively. The power required by the battery for a single cooling plate at Re 400 is 0.00076 W for the CS channel, 0.000125 W for the gradient-1 design, and 0.000106 W for the width-3 design. This makes the width-3 design 13.95% more energy-efficient than the CS channel. **Figure 12** shows the pressure contours at Re 1200 for each channel design. The CS channel design shown in **Figure 12a** exhibits higher pressure at the inlet side compared to the gradient-1 and width-3 designs shown in **Figure 12b** and **Figure 12c**, respectively. Meanwhile, the gradient-1 and width-3 designs have nearly identical pressure contours. In this case, the thermal performance of the width-3 design is superior to that of the CS design but with lower pumping power.

Figure 9 shows the characteristics of each channel design with respect to cooling efficiency coefficient. The higher the cooling efficiency coefficient, the better, as the channel requires less pumping power. At Re 400, the width-3 channel design shows the highest efficiency. When comparing the channels, the highest (width-3) and lowest (CS) efficiency designs show a difference of up to 504.43 at Re 400. This phenomenon is due to

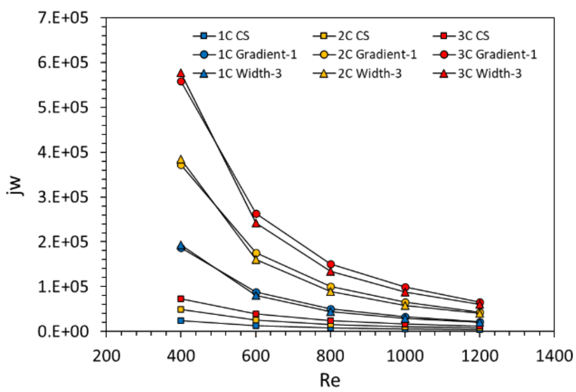

Figure 9. Effect of channel variation on cooling efficiency coefficient

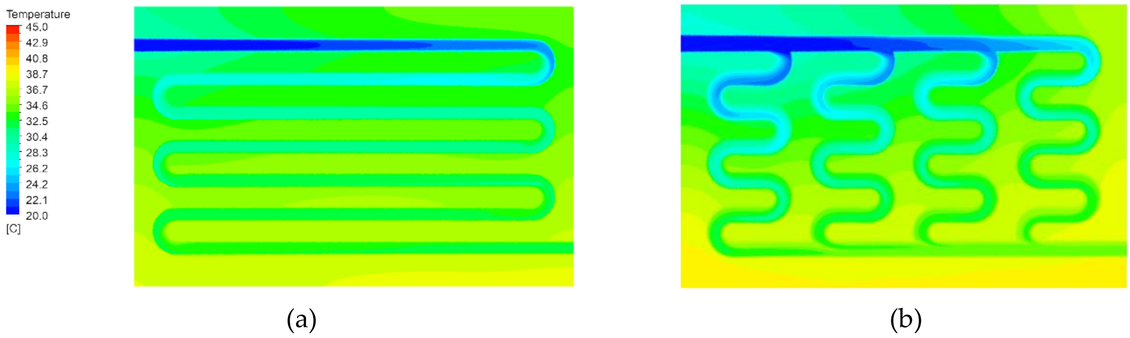

Figure 10. Temperature contours for each channel variation at Re 400 and 3 C C-rate: (a) CS channel design, and (b) width-3 channel design

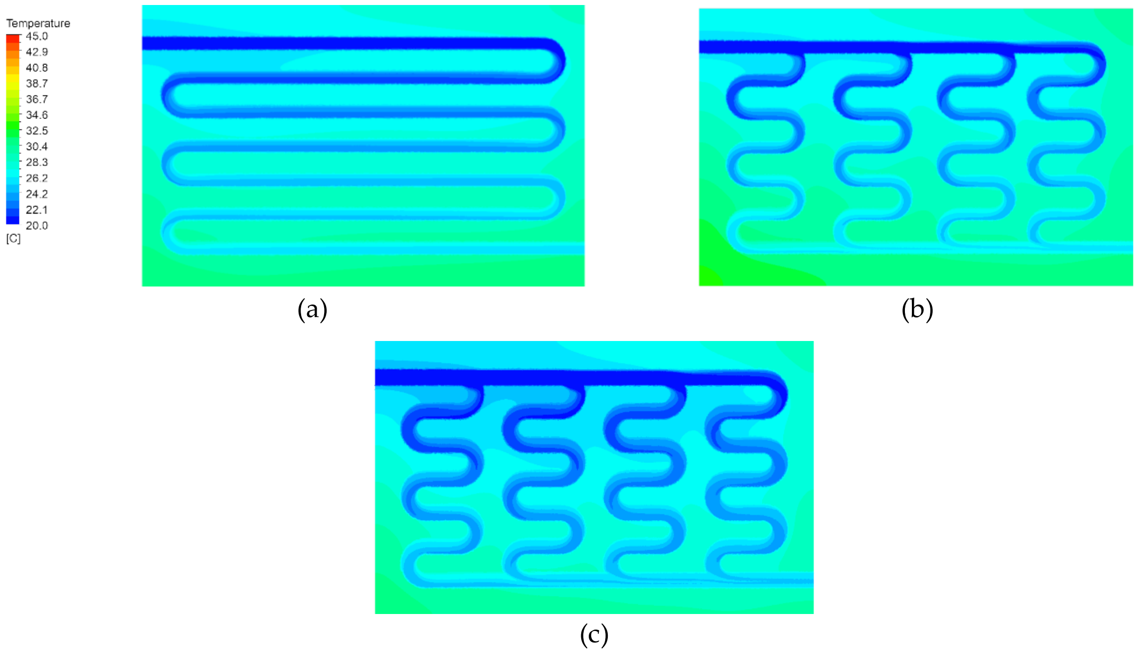

Figure 11. Temperature contours for each channel variation at Re 1200 and 3 C C-rate: (a) CS channel design, (b) gradient-1 channel design, and (c) width-3 channel design

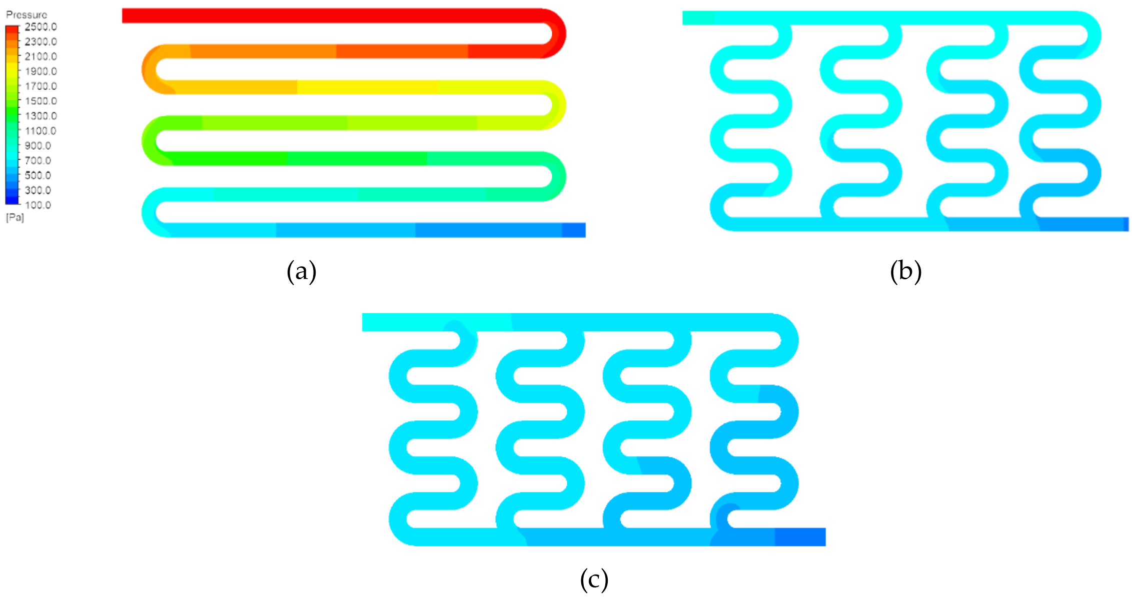

Figure 12. Pressure contours for each channel variation at Re 1200 and 3 C C-rate: (a) CS channel design, (b) gradient-1 channel design, and (c) width-3 channel design

the CS channel design requiring high pumping power. On the other hand, both the gradient-1 and width-3 channel designs require lower pumping power compared to the CS design. The proposed channel design performs better than the CS design due to its lower pumping power requirement.

4. Conclusion

This study investigates serpentine minichannel channels with the addition of branches. The objective of this research is to improve the conventional serpentine channel (CS), which has good thermal performance but requires high pumping power. The results of the study are discussed and analysed, leading to the following conclusions:

- The addition of a gradient improved thermal performance, both in terms of the maximum battery temperature and temperature distribution. Specifically, the gradient reduced $T_{max}{}^{*}$ by 0.07 and T_{σ} by 0.42 compared to the initial channel design (without gradient) at Re 400 and 3 C C-rate. Despite the improved thermal performance, both the gradient and non-gradient channels required nearly the same pumping power.
- Variations in the channel width influenced the thermal performance of the cooling plate. The performance improvement from the design with the smallest and largest channel diameters resulted in reductions of 0.57 and 1.53 for $T_{max}{}^{*}$ and T_{σ} respectively, at Re 400 and 3 C C-rate.
- At Re 1000 and 3 C C-rate, the width-3 channel design outperforms the CS channel design. The reduction in $T_{max}{}^{*}$ for the width-3 channel design compared to the CS channel design is 0.017. Furthermore, the width-3 channel design shows a improvement in the friction factor (f), with a reduction of 0.0149.
- The proposed channel design offers a cooling efficiency coefficient is 504.43 higher than that of the CS channel design.

The findings of this study highlight that the proposed channel design achieves a maximum temperature response and temperature uniformity comparable to that of the conventional serpentine channel. Despite the similarity in thermal performance, the proposed design requires less power than the conventional serpentine channel. However, this study has certain limitations. The limitations in the study are the conditions and measured values of the EV battery are taken based on the cooling plate and the steady-state approach that does not see the dynamic conditions of the battery. Consequently, this study could only approximate the EV battery's characteristics under real conditions. Future research could include the addition of batteries to observe more detailed phenomena. Further studies could also explore the cooling performance under real conditions with transient responses and varying environmental factors.

Acknowledgments

The authors thank to the Ministry of Higher Education, Science, and Technology (Kemendikti Saintek) Republic of Indonesia, PT.VKTR Teknologi Mobilitas Tbk, and Politeknik Elektronika Negeri Surabaya for supporting this research.

Author's Declaration

Authors' contributions and responsibilities

The authors made substantial contributions to the conception and design of the study. The authors took responsibility for data analysis, interpretation and discussion of results. The authors read and approved the final manuscript.

Funding

The research was funded by Ministry of Higher Education, Science, and Technology (Kemendikti Saintek) Republic of Indonesia.

Availability of data and materials

All data are available from the authors.

Competing interests

The authors declare no competing interest.

Additional information

No additional information from the authors.

References

[1] H. Fathabadi, "A novel design including cooling media for Lithium-ion batteries pack used in hybrid and electric vehicles," *Journal of Power Sources*, vol. 245, pp. 495–500, Jan. 2014, doi: 10.1016/j.jpowsour.2013.06.160.

[2] I. C. Setiawan and M. Setiyo, "Renewable and Sustainable Green Diesel (D100) for Achieving Net Zero Emission in Indonesia Transportation Sector," *Automotive*

Experiences, vol. 5, no. 1, pp. 1–2, Mar. 2022, doi: 10.31603/ae.6895.

[3] T. Raja, M. Setiyo, V. Murugan, and S. Dhandapani, "Analysis of the Temperature Variation of Bizarre Thermal Barrier Coatings and their impacts on Engine," *Automotive Experiences*, vol. 6, no. 3, pp. 497–514, Nov. 2023, doi: 10.31603/ae.9802.

[4] T. H. Ariwibowo and A. Miyara, "Thermal Characteristics of Slinky-Coil Ground Heat Exchanger with Discrete Double Inclined Ribs," *Resources*, vol. 9, no. 9, p. 105, Aug. 2020, doi: 10.3390/resources9090105.

[5] L. Z. Ouyang *et al.*, "Low-cost method for sodium borohydride regeneration and the energy efficiency of its hydrolysis and regeneration process," *Journal of Power Sources*, vol. 269, pp. 768–772, Dec. 2014, doi: 10.1016/j.jpowsour.2014.07.074.

[6] G. Guo, B. Long, B. Cheng, S. Zhou, P. Xu, and B. Cao, "Three-dimensional thermal finite element modeling of lithium-ion battery in thermal abuse application," *Journal of Power Sources*, vol. 195, no. 8, pp. 2393–2398, Apr. 2010, doi: 10.1016/j.jpowsour.2009.10.090.

[7] A. R. Abrari, T. H. Ariwibowo, D. Pramadihanto, N. R. Arini, and R. S. Dewanto, "Thermodynamic Analysis of Battery Thermal Management System in Electric Van for Tropical Climate: A Preliminary Study," in *2024 International Electronics Symposium (IES)*, Denpasar, Indonesia, 2024, pp. 66–71, doi: 10.1109/IES63037.2024.10665770.

[8] S. Zhu, A. Huang, and Y. Xu, "Improving Methods for better Performance of Commercial LiFePO4/C Batteries," *International Journal of Electrochemical Science*, vol. 16, no. 5, p. 210564, May 2021, doi: 10.20964/2021.05.49.

[9] R. E. Williford, V. V. Viswanathan, and J.-G. Zhang, "Effects of entropy changes in anodes and cathodes on the thermal behavior of lithium ion batteries," *Journal of Power Sources*, vol. 189, no. 1, pp. 101–107, Apr. 2009, doi: 10.1016/j.jpowsour.2008.10.078.

[10] M. A. Fitrony, T. H. Ariwibowo, M. R. Rusli, E. H. Binugroho, and D. Pramadihanto, "A Thermal Investigation of Heat Sink with Dimple in Battery Cooling for Electric Motorbike Application," in *2024 International Electronics Symposium (IES)*, Denpasar, Indonesia, 2024, pp. 1–6, doi: 10.1109/IES63037.2024.10665800.

[11] H. Liu, H. Shi, H. Shen, and G. Xie, "The performance management of a Li-ion battery by using tree-like mini-channel heat sinks: Experimental and numerical optimization," *Energy*, vol. 189, p. 116150, Dec. 2019, doi: 10.1016/j.energy.2019.116150.

[12] X. Liu, T. Feng, S. Chen, and H. Wei, "Effects of Different Templates on Electrochemical Performance of LiFePO4/C Prepared by Supercritical Hydrothermal Method," *International Journal of Electrochemical Science*, vol. 11, no. 3, pp. 2276–2283, 2016, doi: 10.1016/S1452-3981(23)16101-3.

[13] A. A. Pesaran, "Battery thermal models for hybrid vehicle simulations," *Journal of Power Sources*, vol. 110, no. 2, pp. 377–382, Aug. 2002, doi: 10.1016/S0378-7753(02)00200-8.

[14] Z. Xiao, G. Hu, K. Du, and Z. Peng, "Improving electrochemical performances of LiFePO4/C cathode material via a novel three-layer electrode," *Transactions of Nonferrous Metals Society of China*, vol. 23, no. 11, pp. 3324–3329, Nov. 2013, doi: 10.1016/S1003-6326(13)62871-X.

[15] W. Waag and D. U. Sauer, "Adaptive estimation of the electromotive force of the lithium-ion battery after current interruption for an accurate state-of-charge and capacity determination," *Applied Energy*, vol. 111, pp. 416–427, Nov. 2013, doi: 10.1016/j.apenergy.2013.05.001.

[16] Z. Rao and S. Wang, "A review of power battery thermal energy management," *Renewable and Sustainable Energy Reviews*, vol. 15, no. 9, pp. 4554–4571, Dec. 2011, doi: 10.1016/j.rser.2011.07.096.

[17] O. Kalkan, A. Celen, and K. Bakirci, "Experimental and numerical investigation of the LiFePO4 battery cooling by natural convection," *Journal of Energy Storage*, vol. 40, p. 102796, Aug. 2021, doi: 10.1016/j.est.2021.102796.

[18] O. Kalkan, A. Celen, K. Bakirci, and A. S. Dalkilic, "Experimental investigation of thermal performance of novel cold plate

design used in a Li-ion pouch-type battery," *Applied Thermal Engineering*, vol. 191, p. 116885, Jun. 2021, doi: 10.1016/j.applthermaleng.2021.116885.

[19] W. Wu, S. Wang, W. Wu, K. Chen, S. Hong, and Y. Lai, "A critical review of battery thermal performance and liquid based battery thermal management," *Energy Conversion and Management*, vol. 182, pp. 262–281, Feb. 2019, doi: 10.1016/j.enconman.2018.12.051.

[20] K. Monika and S. P. Datta, "Comparative assessment among several channel designs with constant volume for cooling of pouch-type battery module," *Energy Conversion and Management*, vol. 251, p. 114936, Jan. 2022, doi: 10.1016/j.enconman.2021.114936.

[21] G. Zhao, X. Wang, M. Negnevitsky, and C. Li, "An up-to-date review on the design improvement and optimization of the liquid-cooling battery thermal management system for electric vehicles," *Applied Thermal Engineering*, vol. 219, p. 119626, Jan. 2023, doi: 10.1016/j.applthermaleng.2022.119626.

[22] X. Mo, H. Zhi, Y. Xiao, H. Hua, and L. He, "Topology optimization of cooling plates for battery thermal management," *International Journal of Heat and Mass Transfer*, vol. 178, p. 121612, Oct. 2021, doi: 10.1016/j.ijheatmasstransfer.2021.121612.

[23] Y. Huang *et al.*, "A novel approach for Lithium-ion battery thermal management with streamline shape mini channel cooling plates," *Applied Thermal Engineering*, vol. 157, p. 113623, Jul. 2019, doi: 10.1016/j.applthermaleng.2019.04.033.

[24] Y. Huo, Z. Rao, X. Liu, and J. Zhao, "Investigation of power battery thermal management by using mini-channel cold plate," *Energy Conversion and Management*, vol. 89, pp. 387–395, Jan. 2015, doi: 10.1016/j.enconman.2014.10.015.

[25] H. Liu, X. Gao, J. Zhao, M. Yu, D. Niu, and Y. Ji, "Liquid-based battery thermal management system performance improvement with intersected serpentine channels," *Renewable Energy*, vol. 199, pp. 640–652, Nov. 2022, doi: 10.1016/j.renene.2022.09.026.

[26] S. Lin and L. Zhou, "Thermal performance of rectangular serpentine mini-channel cooling system on lithium battery," *Journal of Cleaner Production*, vol. 418, p. 138125, Sep. 2023, doi: 10.1016/j.jclepro.2023.138125.

[27] T. Deng, G. Zhang, and Y. Ran, "Study on thermal management of rectangular Li-ion battery with serpentine-channel cold plate," *International Journal of Heat and Mass Transfer*, vol. 125, pp. 143–152, Oct. 2018, doi: 10.1016/j.ijheatmasstransfer.2018.04.065.

[28] H. M. Jaffal, N. S. Mahmoud, A. A. Imran, and A. Hasan, "Performance enhancement of a novel serpentine channel cooled plate used for cooling of Li-ion battery module," *International Journal of Thermal Sciences*, vol. 184, p. 107955, Feb. 2023, doi: 10.1016/j.ijthermalsci.2022.107955.

[29] S. Sun, C. Ma, X. Wang, Y. Yang, and J. Mei, "Design and optimisation of a novel serpentine flow channel with branch structure," *Energy*, vol. 293, p. 130494, Apr. 2024, doi: 10.1016/j.energy.2024.130494.

[30] N. Wang, C. Li, W. Li, X. Chen, Y. Li, and D. Qi, "Heat dissipation optimization for a serpentine liquid cooling battery thermal management system: An application of surrogate assisted approach," *Journal of Energy Storage*, vol. 40, p. 102771, Aug. 2021, doi: 10.1016/j.est.2021.102771.

[31] L. Fan, J. Li, Y. Chen, D. Zhou, Z. Jiang, and J. Sun, "Study on the cooling performance of a new secondary flow serpentine liquid cooling plate used for lithium battery thermal management," *International Journal of Heat and Mass Transfer*, vol. 218, p. 124711, Jan. 2024, doi: 10.1016/j.ijheatmasstransfer.2023.124711.

[32] Md. H. ALI and A. MIYARA, "Analysis of Optimum Slinky Loop Arrangement for Horizontal Ground Heat Exchanger." Japan Society of Refrigerating and Air Conditioning Engineers, 31-Dec-2017 [Online]. Available: https://doi.org/10.11322/tjsrae.17-55HE. [Accessed: 22-Nov-2024]

[33] EVE Battery, "LF80 LFP Power Battery Product Specification," LF80-73103, Aug. 2018.

[34] I. H. Bell, J. Wronski, S. Quoilin, and V. Lemort, "Pure and Pseudo-pure Fluid Thermophysical Property Evaluation and the Open-Source Thermophysical Property Library CoolProp," *Ind. Eng. Chem. Res.*, vol. 53, no. 6, pp. 2498–2508, Feb. 2014, doi: 10.1021/ie4033999.

[35] J. Tu, G.-H. Yeoh, and C. Liu, "Governing Equations for CFD: Fundamentals," in *Computational Fluid Dynamics*, Elsevier, 2018, pp. 65–124 [Online]. Available: https://linkinghub.elsevier.com/retrieve/pii/B9780081011270000039. [Accessed: 22-Nov-2024]

[36] L. Rao and J. Newman, "Heat-Generation Rate and General Energy Balance for Insertion Battery Systems," *J. Electrochem. Soc.*, vol. 144, no. 8, pp. 2697–2704, Aug. 1997, doi: 10.1149/1.1837884.

[37] X. Qian, D. Xuan, X. Zhao, and Z. Shi, "Heat dissipation optimization of lithium-ion battery pack based on neural networks," *Applied Thermal Engineering*, vol. 162, p. 114289, Nov. 2019, doi: 10.1016/j.applthermaleng.2019.114289.

[38] Y. Shi, S. Ahmad, H. Liu, K. T. Lau, and J. Zhao, "Optimization of air-cooling technology for LiFePO4 battery pack based on deep learning," *Journal of Power Sources*, vol. 497, p. 229894, Jun. 2021, doi: 10.1016/j.jpowsour.2021.229894.

[39] A. Jarrett and I. Y. Kim, "Influence of operating conditions on the optimum design of electric vehicle battery cooling plates," *Journal of Power Sources*, vol. 245, pp. 644–655, Jan. 2014, doi: 10.1016/j.jpowsour.2013.06.114.

[40] T. L. Bergman, A. Lavine, and F. P. Incropera, *Fundamentals of heat and mass transfer*, Eighth edition. Wiley abridged print companion. Hoboken, NJ: John Wiley & Sons, Inc., 2019.

[41] J. Tu, G.-H. Yeoh, and C. Liu, "CFD Mesh Generation: A Practical Guideline," in *Computational Fluid Dynamics*, Elsevier, 2018, pp. 125–154 [Online]. Available: https://linkinghub.elsevier.com/retrieve/pii/B9780081011270000040. [Accessed: 22-Nov-2024].